

Photochemistry

Water Oxidation under Modal Ultrastrong Coupling Conditions Using Gold/Silver Alloy Nanoparticles and Fabry–Pérot Nanocavities

Yoshiki Suganami, Tomoya Oshikiri, Xu Shi, and Hiroaki Misawa*

How to cite: *Angew. Chem. Int. Ed.* **2021**, *60*, 18438–18442

International Edition: doi.org/10.1002/anie.202103445

German Edition: doi.org/10.1002/ange.202103445

Abstract: We developed a photoanode consisting of Au-Ag alloy nanoparticles (NPs), a TiO₂ thin film and a Au film (AATA) under modal strong coupling conditions with a large splitting energy of 520 meV, which can be categorized into the ultrastrong coupling regime. We fabricated a photoanode under ultrastrong coupling conditions to verify the relationship between the coupling strength and photoelectric conversion efficiency and successfully performed efficient photochemical reactions. The AATA photoanode showed a 4.0% maximum incident photon-to-current efficiency (IPCE), obtained at 580 nm, and the internal quantum efficiency (IQE) was 4.1%. These results were attributed to the high hot-electron injection efficiency due to the larger near-field enhancement and relatively negative potential distribution of the hot electrons. Furthermore, hybrid mode-induced water oxidation using AATA structures was performed, with a Faraday efficiency of more than 70% for O₂ evolution.

To realize a sustainable society that does not depend on fossil fuels, development of an artificial photosynthesis system that produces hydrogen and oxygen from water using visible light, a major component of sunlight, is extremely important. As photoanodes for overall water splitting systems using visible light, metal nanoparticle (NP)-decorated semiconductor systems that exhibit visible light-harvesting effects induced by localized surface plasmon resonance (LSPR) have attracted considerable attention.^[1–7] Such plasmonic metal NPs not only serve as light-harvesting units but also promote plasmon-induced hot electron and hot hole (hot carrier) generation,^[8,9] and the charge separation of these hot carriers

occurs at the metal/semiconductor interface, followed by reduction/oxidation reactions.^[10–12] For example, gold nanoparticle (Au NP)-loaded titanium dioxide (TiO₂) has been shown to function as a stable photoanode for water oxidation under irradiation by light with wavelengths longer than 550 nm in the presence of an electrical or chemical bias without noticeable loss of activity.^[13–17] However, the LSPR of single-layer Au NPs on a TiO₂ substrate cannot realize sufficient broadband light absorption, and the quantum yield of the water oxidation reaction is still low.^[18]

Recently, we developed a new photoanode that utilized strong coupling between LSPR and Fabry–Pérot (FP) nanocavities to overcome the challenges associated with plasmonic water splitting. The photoanode exhibiting strong coupling consists of Au NPs/TiO₂ thin film/Au film (ATA). Strong coupling is induced when the resonant wavelengths of the nanocavity and the LSPR of the Au NPs match each other closely.^[19] The hybrid states generated under strong coupling appear at shorter and longer wavelengths than the original resonant wavelengths of the nanocavity and the LSPR of the Au NPs,^[20,21] which broadens the absorption wavelength range and results in efficient absorption.^[22] More interestingly, the quantum yield of photocurrent generation based on water oxidation was demonstrated to be 1.5 times larger than that of the traditional plasmonic photoanode without strong coupling. However, the mechanism underlying the quantum yield enhancement under modal strong coupling is still uncertain. We speculated that the coupling strength between the LSPR of metal NPs and the FP nanocavity affects the quantum yields under modal strong coupling conditions.

In this study, to understand hot-electron injection phenomena under strong coupling conditions with extremely high splitting energies, the so-called ultrastrong coupling condition, we focused on the oscillator strength of the LSPR. The splitting energy $\hbar\Omega$, which represents the coupling strength in light-matter coupling, is related to the oscillator strength of the resonators as:^[23]

$$\hbar\Omega \propto \sqrt{Nf} \quad (1)$$

where N and f are the number of oscillators and oscillator strength, respectively. Here, we speculated that the splitting energy of the modal strong coupling system also increases with increasing LSPR oscillator strength.

Generally, the oscillator strength of the LSPR of metal NPs increases as the imaginary part of their dielectric constant decreases.^[24] Since the imaginary part of the dielectric constant of Ag is smaller than that of Au at all visible wavelengths,^[25] the oscillator strength of the LSPR of Ag NPs is larger than that of Au NPs.^[26] However, Ag NPs are

[*] Y. Suganami, Dr. T. Oshikiri, Dr. X. Shi, Prof. H. Misawa
Research Institute for Electronic Science, Hokkaido University
N21, W10, Kita-ku, Sapporo 001–0021 (Japan)
E-mail: misawa@es.hokudai.ac.jp

Prof. H. Misawa
Center for Emergent Functional Matter Science
National Yang Ming Chiao Tung University
Hsinchu, 30010 (Taiwan)

Dr. X. Shi
Present address: Creative Research Institution, Hokkaido University
N21, W10, Kita-ku, Sapporo 001–0021 (Japan)

Supporting information and the ORCID identification number(s) for the author(s) of this article can be found under:
<https://doi.org/10.1002/anie.202103445>.

© 2021 The Authors. Angewandte Chemie International Edition published by Wiley-VCH GmbH. This is an open access article under the terms of the Creative Commons Attribution Non-Commercial NoDerivs License, which permits use and distribution in any medium, provided the original work is properly cited, the use is non-commercial and no modifications or adaptations are made.

easily oxidized, which hinders their use in the photooxidation of water.^[27] Therefore, we employed Au-Ag alloy NPs with a high oscillator strength and sufficient durability against oxidation reactions^[28–31] to construct a photoanode under ultrastrong coupling conditions for efficient photochemical water splitting. From optical measurements, we found that this photoanode presents a splitting energy of up to 620 meV, which can be categorized into the ultrastrong coupling regime.^[32,33,37] In addition, during photocurrent measurements using this photoanode, only Ag on the surface of the Au-Ag alloy NPs eluted in the very early stage of the reaction, and a long-term stable photocurrent was observed. Moreover, under the ultrastrong coupling conditions when using Au-Ag alloy NPs, the observed photocurrent was demonstrated to be larger than that under the strong coupling conditions when using Au NPs.

The Au-Ag alloy NP/TiO₂/Au film (AATA) structure shown in the schematic diagram in Figure 1a was fabricated. The TiO₂/Au film serves as an FP nanocavity because TiO₂

has a large refractive index (2.4 at 600 nm), and a phase change occurs due to the reflection at the TiO₂/Au film interface (Supporting Information, Figure S1a).^[20,34,35] The LSPR of the Au-Ag alloy NPs has a larger oscillator strength than that of the Au NPs, as mentioned above, and was therefore used to increase the strength of the coupling with the nanocavity. Au-Ag alloy NPs with 30 at% Ag were prepared by annealing Au and Ag thin films with thicknesses of 3.5 and 1.5 nm, respectively. The average particle size determined from scanning electron microscopy (SEM) images was 21 nm (Figure S2). A cross-sectional view (Figure 1b) of the sample was acquired by scanning transmission electron microscopy (STEM). A periodic lattice structure was clearly observed, indicating the high crystallinity of the NPs. The energy-dispersive X-ray spectrometry (EDS) mapping shown in Figure 1c shows that Au and Ag atoms were uniformly dispersed in the NPs. Furthermore, we coated the Au-Ag alloy NPs with TiO₂ with a thickness of 7 nm because the coupling between the LSPR and FP nanocavity modes is known to be enhanced by a larger spatial overlap between the two modes.^[20]

Figure 1d shows the absorption spectra of the AATA structures with different TiO₂ thicknesses. The absorption spectra were obtained by measuring the reflectance *R* and calculating $-\log(R)$ as a function of wavelength. Under these experimental conditions, the transmittance was always zero, as confirmed by UV/Vis spectroscopy. The absorption spectra showed two peaks attributed to two new hybrid modes (*P*₊, *P*₋) due to the formation of strong coupling between the LSPR and cavity modes. A third component was also observed in Figure 1d and was attributed to the uncoupled FP cavity mode.^[36] The dispersion curve was generated by plotting the energy of *P*₊ and *P*₋ as a function of the cavity wavenumber, as shown in Figure 1e. The splitting energy $\hbar\Omega$ was calculated to be 620 meV by using a coupled harmonic oscillator model, as described by Equation (2), and this value was almost twice that determined for ATA with an average size of 12 nm in previous research.^[20]

$$E_{\pm}(\delta) = \frac{E_p + E_c}{2} \pm \frac{1}{2} \sqrt{(E_p - E_c)^2 + |\hbar\Omega|^2} \quad (2)$$

where E_{\pm} are the energies of *P*₊ and *P*₋ and E_c and E_p are the energies of the cavity and LSPR modes, respectively. Figure 1f shows the energy diagram of AATA. When the cavity mode matches the LSPR of the Au-Ag alloy NPs, hybrid modes with upper and lower branches are formed.

The photoelectrochemical performance of the AATA photoanode was evaluated by measuring the photocurrent based on the oxidation of water. As a comparison, we also measured the photocurrent using the ATA photoanode. To remove silver oxide from the surface of the Au-Ag alloy NPs, the samples were submerged in a 19 wt% NH₃ aqueous solution for 3 min before depositing an additional TiO₂ layer. In these cases, the Au NPs and Au-Ag alloy NPs were partially inlaid in TiO₂ at a depth of 7 nm to maintain the three-phase boundaries of metal, TiO₂, and water (Figure 2a). The splitting energies for the AATA and ATA anodes were calculated as 520 meV and 350 meV, respectively (Figure S3).

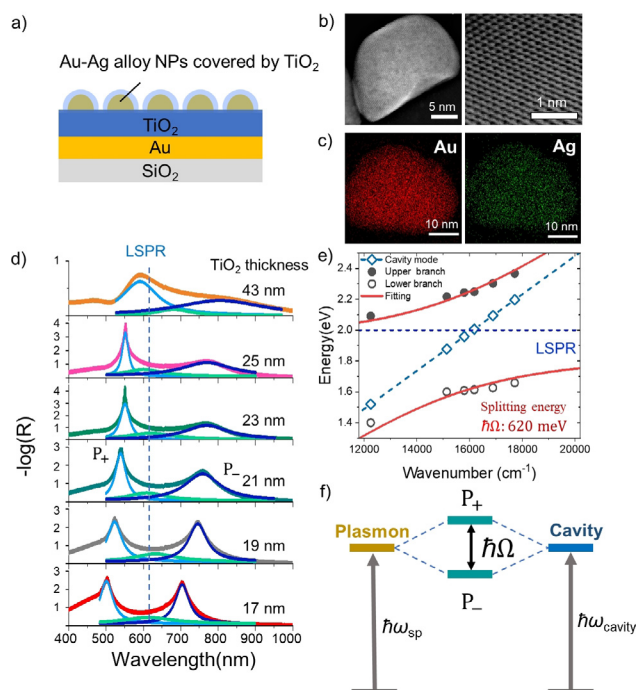


Figure 1. a) AATA with inlaid Au-Ag alloy NPs. The average size of the Au-Ag alloy NPs was 21 nm. b) Cross-sectional STEM image of Au-Ag alloy NPs (left), and magnified view of the left panel revealing the lattice structure (right). c) EDS mappings of the cross section of a Au-Ag alloy NP. The red and green dots represent Au and Ag, respectively. d) Absorption spectra of AATA structures with varying TiO₂ thicknesses. The alloy NP inlay depth was 7 nm. The cyan, navy, and green curves indicate the Lorentz fitting of the three components. e) Dispersion curve of hybrid modes in the AATA structures. The energies of the coupling conditions were determined from the absorption spectra in panel d). The red curves show the fitting using a coupled harmonic oscillator model. The blue dashed line shows the LSPR energy of the Au-Ag alloy NPs. The green dashed line displays only the cavity mode of a TiO₂/Au film. f) Energy-level diagram of the modal strong coupling between the cavity mode and the LSPR of the Au-Ag alloy NPs. ω_{sp} and ω_{cavity} are the resonant frequencies of the LSPR and FP nanocavity modes, respectively.

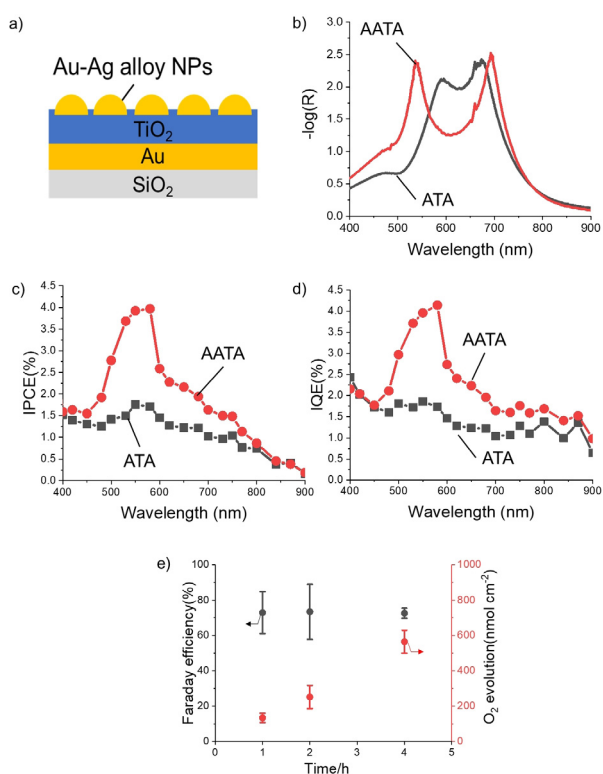


Figure 2. a) AATA with partially inlaid Au-Ag alloy NPs. b) Absorption spectra of AATA and ATA with TiO₂ thicknesses of 21 nm and 28 nm and Au-Ag alloy NP and Au NP sizes of 20 nm and 12 nm, respectively. The Au-Ag alloy NPs and Au NPs were partially inlaid in the nanocavity at an inlay depth of 7 nm. IPCE c) and IQE d) action spectra of AATA and ATA photoanodes. The applied potential was 0.5 V vs. Ag/AgCl. The black and red lines indicate AATA and ATA structures, respectively. e) Irradiation time dependence of the Faraday efficiency and O₂ evolution using the AATA photoanode at 0.5 V vs. Ag/AgCl under visible light irradiation ($\lambda > 400$ nm, 550 mWcm⁻²). The irradiation light area was 4.0 mm². The Faraday efficiency and O₂ evolution are plotted in black and red, respectively.

When the resonance energies of the LSPR and the cavity correspond to a $\hbar\omega_0$ of 2060 meV under the uncoupled condition, the energy relationship of the AATA structure is $\hbar\Omega = 0.25 \hbar\omega_0$. This result indicates that the AATA structure fulfils the ultrastrong coupling condition, which is defined as $\hbar\Omega > 0.2 \hbar\omega_0$, as discussed for both modal and light-matter coupling.^[32,37] Figures 2b and 2c show the absorption and incident photon-to-current efficiency (IPCE) action spectra of the AATA and ATA photoanodes. Before starting the IPCE measurement, the photoanodes were irradiated with 580 nm light for 2 hours to remove Ag from the surface of the Au-Ag alloy NPs. From the optical spectra (Figure S4a), SEM images (Figure S4b), and time-current curve (Figure S4c), the elution of Ag was confirmed to stop after 2 hours of light irradiation at 580 nm. The IPCEs of AATA were significantly higher than those of ATA in the visible light wavelength range, especially from 500 to 600 nm. The highest IPCE for AATA was approximately 2.4 times that of ATA, and the average IPCE from 400 nm to 800 nm increased by 1.7 times. Furthermore, the internal quantum efficiency (IQE) spectra were calculated by dividing the IPCE spectrum by $1-R$ to

determine the charge separation efficiency (Figure 2d). The IQEs of AATA were higher than those of ATA at wavelengths from 420 nm to 900 nm. The AATA photoanode showed a maximum IPCE of 4.0% at 580 nm, and the IQE at the same wavelength was 4.1%. The IQE enhancements of AATA compared to ATA at the peaks of the upper and lower branches (at 580 nm and 700 nm) were 2.4 and 1.6 times, respectively.

An AATA photoanode with 21 nm TiO₂ and Au-Ag alloy NPs at a 7 nm inlay depth was used for the water oxidation reaction in a three-electrode system to directly verify that the photocurrent is derived from oxygen evolution based on water oxidation rather than from Ag oxidation. Figure 2e shows the irradiation-time dependence of the oxygen evolution and the Faraday efficiency under visible light irradiation with wavelengths longer than 400 nm. Before the measurement, this photoanode was irradiated with 580 nm light for 2 hours to remove Ag from the surface of Au-Ag alloy NPs. An aqueous KOH solution with ¹⁸O water (16.2 at % isotopic purity) was used to quantify the O₂ evolution. The amount of oxygen generated was almost proportional to the reaction time, and the Faraday efficiency for O₂ evolution was approximately 74% throughout the reaction. The results showed that the photocurrent was mainly derived from the oxidation of water rather than from that of Ag, indicating that the Au-Ag alloy NPs could be stably used for the water oxidation reaction.

To explore why the IQE of the AATA photoanode is higher than that of ATA, we performed transient absorption measurements. Since measuring the transient absorption of thin films with the thickness of the TiO₂ film is difficult due to the weak absorption, AATA and ATA with thicker TiO₂ films, whose second-order FP nanocavity (Figure S1b) coupled with the LSPRs of Au-Ag alloy NPs and Au NPs, respectively, were used for the measurements. Figures 3a and 3b show the time profiles of the transient absorption signals pumped at different wavelengths. Figures 3c and 3d show the maximum transient signals of AATA and ATA, respectively. The maximum ΔOD (ΔOD_{Max}) for each measurement was estimated by extracting the maximum value of the fitted convoluted function of a second-order reaction model that occurred near time zero, that is, temporal overlap between the pump and probe pulses. The ΔOD_{Max} monitored by the probe pulse of 3500 nm represents the total amount of electrons injected into the conduction band of TiO₂. Furthermore, the wavelength dependence of ΔOD_{Max} showed a similar tendency as the IQE action spectra in Figure 2d. A detailed analysis in the decay of the transient measurements is discussed in the supporting information (Figure S5). Therefore, the highly efficient photoelectrochemical reaction on AATA is derived from electron injection from Au-Ag alloy NPs to TiO₂. One of the reasons for the higher electron injection efficiencies of AATA, especially at the upper branch, is the energy distribution of hot electrons. A blueshift of the absorption peak of the upper branch was observed due to the increase in the coupling strength. Additionally, Au alloyed with Ag has been reported to present a shift in the interband energy threshold to a more negative potential.^[29] In fact, the work functions of AATA and ATA were estimated by

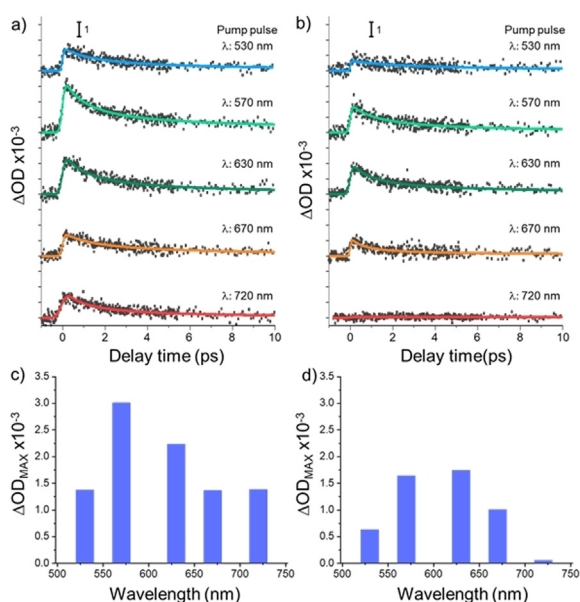


Figure 3. a), b) Time profiles of the transient measurements performed for AATA (a) and ATA (b). The TiO₂ thicknesses on the AATA and ATA photoanodes were 140 nm and 150 nm, respectively. Au-Ag alloy NPs and Au NPs were partially inlaid in the nanocavity at an inlay depth of 7 nm. c), d) The maximum transient signals of AATA (c) and ATA (d). The probe pulse for the transient measurements was 3500 nm. The wavelengths of the pump pulse are indicated in (a) and (b).

photoemission electron spectroscopy to be 4.7 and 5.0 eV, respectively (Figure S6). Both the negative shift of the excitation wavelength and the work function of metallic NPs induce the generation of hot electrons with a relatively negative potential distribution and result in higher hot-electron injection efficiencies.^[38] At the same time, the increase in the IPCE of AATA showed that hot holes with a sufficient positive potential to oxidize water were produced. However, considering that the maximum IPCE of Au-Ag alloy NP/TiO₂ was only 1.7 times that of Au NP/TiO₂ (Figure S7), an additional effect should be considered to explain why the highest IPCE of AATA was 2.4 times that of ATA. The peak intensity of the upper branch of the near-field spectrum for AATA calculated by a numerical simulation was 3.0 times higher than that for ATA even though the peak intensity corresponding to the IPCE peak of the near-field spectrum of Au-Ag alloy NP/TiO₂ was 2.1 times higher than that for Au NP/TiO₂ (Figure S8). The more significant near-field enhancement under modal coupling based on the larger oscillation strength of the LSPR of Au-Ag alloy NPs contributes to efficient electron injection.

In conclusion, we have achieved a splitting energy of 520 meV in the modal coupling between Au-Ag alloy NPs and FP nanocavity modes. This remarkably high splitting energy derives from the large oscillator strength of the LSPR of Au-Ag alloy NPs and fulfils the ultrastrong coupling condition. The maximum IPCE of the AATA photoanode was 2.4-fold higher than that of conventional ATA, and the IQEs at the peaks of the upper and lower branches of the former photoanode were enhanced by 2.4 and 1.6 times, respectively, relative to those of the latter. The highly efficient hot-electron

injection on AATA, which is based on the large near-field enhancement and relatively negative potential distribution of the hot electrons, was directly observed by transient absorption measurements at IR wavelengths. Furthermore, hybrid mode-induced water oxidation using AATA structures was performed, with a Faraday efficiency of more than 70 % for O₂ evolution. This research is the first to report a highly efficient chemical reaction performed under modal ultra-strong coupling conditions.

Acknowledgements

We are grateful to Yuko Mori, Naomi Hirai, and Prof. Yasutaka Matsuo at Hokkaido University for STEM measurements. We are grateful to Dr. Yocef. Hattori at Hokkaido University for the transient measurement analysis. We acknowledge financial support from JSPS KAKENHI (Grant Nos. JP18H05205, JP18K05053, JP20H05083, and JP20K15113), the Nanotechnology Platform (Hokkaido University), and the Dynamic Alliance for Open Innovation Bridging Human, Environment and Materials (Five-Star Alliance) of MEXT. Y.S. acknowledges to the Hokkaido University Ambitious Doctoral Fellowship (Information Science and AI).

Conflict of Interest

The authors declare no conflict of interest.

Keywords: modal strong coupling · nanostructures · photochemistry · surface plasmon resonance · water oxidation

- [1] D. B. Ingram, S. Linc, *J. Am. Chem. Soc.* **2011**, *133*, 5202–5205.
- [2] S. Mubeen, J. Lee, N. Singh, S. Krämer, G. D. Stucky, M. Moskovits, *Nat. Nanotechnol.* **2013**, *8*, 247–251.
- [3] Y. Zhong, K. Ueno, Y. Mori, X. Shi, T. Oshikiri, K. Murakoshi, H. Inoue, H. Misawa, *Angew. Chem. Int. Ed.* **2014**, *53*, 10350–10354; *Angew. Chem.* **2014**, *126*, 10518–10522.
- [4] H. J. Kim, S. H. Lee, A. A. Upadhye, I. Ro, M. I. Tejedor-Tejedor, M. A. Anderson, W. B. Kim, G. W. Huber, *ACS Nano* **2014**, *8*, 10756–10765.
- [5] M. Wu, W. J. Chen, Y. H. Shen, F. Z. Huang, C. H. Li, S. K. Li, *ACS Appl. Mater. Interfaces* **2014**, *6*, 15052–15060.
- [6] P. Zhang, T. Wang, J. Gong, *Adv. Mater.* **2015**, *27*, 5328–5342.
- [7] K. Ueno, T. Oshikiri, H. Misawa, *ChemPhysChem* **2016**, *17*, 199–215.
- [8] K. H. W. Ho, A. Shang, F. Shi, T. W. Lo, P. H. Yeung, Y. S. Yu, X. Zhang, K. Y. Wong, D. Y. Lei, *Adv. Funct. Mater.* **2018**, *28*, 1–10.
- [9] G. C. Li, Q. Zhang, S. A. Maier, D. Lei, *J. Nanophotonics* **2018**, *12*, 1865–1889.
- [10] G. Zhao, H. Kozuka, T. Yoko, *Thin Solid Films* **1996**, *277*, 147–154.
- [11] C. Sönnichsen, T. Franzl, T. Wilk, G. von Plessen, J. Feldmann, O. Wilson, P. Mulvaney, *Phys. Rev. Lett.* **2002**, *88*, 774021–774024.
- [12] C. Clavero, *Nat. Photonics* **2014**, *8*, 95–103.
- [13] Z. Liu, W. Hou, P. Pavaskar, M. Aykol, S. B. Cronin, *Nano Lett.* **2011**, *11*, 1111–1116.
- [14] R. Takakura, T. Oshikiri, K. Ueno, X. Shi, T. Kondo, H. Masuda, H. Misawa, *Green Chem.* **2017**, *19*, 2398–2405.

- [15] Z. Zhang, L. Zhang, M. N. Hedhili, H. Zhang, P. Wang, *Nano Lett.* **2013**, *13*, 14–20.
- [16] S. Wang, Y. Gao, S. Miao, T. Liu, L. Mu, R. Li, F. Fan, C. Li, *J. Am. Chem. Soc.* **2017**, *139*, 11771–11778.
- [17] K. Suzuki, X. Li, Y. Wang, F. Nagasawa, K. Murakoshi, *ACS Energy Lett.* **2020**, *5*, 1252–1259.
- [18] D. C. Ratchford, *ACS Nano* **2019**, *13*, 13610–13614.
- [19] C. Hägglund, G. Zeltzer, R. Ruiz, A. Wangperawong, K. E. Roelofs, S. F. Bent, *ACS Photonics* **2016**, *3*, 456–463.
- [20] X. Shi, K. Ueno, T. Oshikiri, Q. Sun, K. Sasaki, H. Misawa, *Nat. Nanotechnol.* **2018**, *13*, 953–958.
- [21] S. Chen, G. Li, D. Lei, K. W. Cheah, *Nanoscale* **2013**, *5*, 9129–9133.
- [22] Y. L. Wong, H. Jia, A. Jian, D. Lei, A. I. El Abed, X. Zhang, *Nanoscale* **2021**, *13*, 2792–2800.
- [23] M. Suzuki, K. Nishiyama, N. Kani, X. Yu, K. Uzumi, M. Funahashi, F. Shimokawa, S. Nakanishi, N. Tsurumachi, *Appl. Phys. Lett.* **2019**, *114*, 191108.
- [24] B. Tandon, S. Ghosh, D. J. Milliron, *Chem. Mater.* **2019**, *31*, 7752–7760.
- [25] D. Rioux, S. Vallières, S. Besner, P. Muñoz, E. Mazur, M. Meunier, *Adv. Opt. Mater.* **2014**, *2*, 176–182.
- [26] R. Thomas, A. Thomas, S. Pullanchery, L. Joseph, S. M. Somasundaran, R. S. Swathi, S. K. Gray, K. G. Thomas, *ACS Nano* **2018**, *12*, 402–415.
- [27] Y. Ohko, T. Tatsuma, T. Fujii, K. Naoi, C. Niwa, Y. Kubota, A. Fujishima, *Nat. Mater.* **2003**, *2*, 29–31.
- [28] S. Link, M. A. El-Sayed, *J. Phys. Chem. B* **1999**, *103*, 8410–8426.
- [29] M. Valenti, A. Venugopal, D. Tordera, M. P. Jonsson, G. Biskos, A. Schmidt-Ott, W. A. Smith, *ACS Photonics* **2017**, *4*, 1146–1152.
- [30] C. Gao, Y. Hu, M. Wang, M. Chi, Y. Yin, *J. Am. Chem. Soc.* **2014**, *136*, 7474–7479.
- [31] D. Y. Lei, J. Li, H. C. Ong, *Appl. Phys. Lett.* **2007**, *91*, 2005–2008.
- [32] W. Gao, X. Li, M. Bamba, J. Kono, *Nat. Photonics* **2018**, *12*, 362–368.
- [33] P. Forn-Díaz, L. Lamata, E. Rico, J. Kono, E. Solano, *Rev. Mod. Phys.* **2019**, *91*, 25005.
- [34] C. Wu, B. Neuner, G. Shvets, J. John, A. Milder, B. Zollars, S. Savoy, *Phys. Rev. B Condens. Matter Mater. Phys.* **2011**, *84*, 075102.
- [35] M. A. Schmidt, D. Y. Lei, L. Wondraczek, V. Nazabal, S. A. Maier, *Nat. Commun.* **2012**, *3*, 1108.
- [36] X. Xiong, J. Bin You, P. Bai, C. E. Png, Z. K. Zhou, L. Wu, *J. Nanophotonics* **2019**, *13*, 257–266.
- [37] D. G. Baranov, B. Munkhbat, E. Zhukova, A. Bisht, A. Canales, B. Rousseaux, G. Johansson, T. J. Antosiewicz, T. Shegai, *Nat. Commun.* **2020**, *11*, 2715.
- [38] H. Nishi, T. Torimoto, T. Tatsuma, *Phys. Chem. Chem. Phys.* **2015**, *17*, 4042–4046.

Manuscript received: March 9, 2021

Revised manuscript received: May 27, 2021

Accepted manuscript online: June 17, 2021

Version of record online: July 21, 2021